ACS NANO

www.acsnano.org

ARTICLE

Nanoscopic Imaging of Biogenic Feedstock-Induced Corrosion in Model Petroleum Infrastructure

Zhiheng Lyu, Samyukta Shrivastav, Jiahui Li, Chang Qian, Lehan Yao, Nachi Shah, Maryam Eslami, Chang Liu, Sheila Ismail, John Shabaker, Eric Doskocil, Daniel V. Krogstad, Jessica A. Krogstad, and Qian Chen*

Cite This: https://doi.org/10.1021/acsnano.5c06142

Read Online

ACCESS | Metrics & More | Article Recommendations | Supporting Information

ABSTRACT: **Biofeedstocks derived from living organisms or their byproducts have recently emerged as an environmentally benign complement to petroleum, diversifying energy production in the petroleum industry from sole dependence on crude oil while utilizing mostly existing petroleum infrastructure. However, biofeedstocks also bring challenges as they can cause distinct and potentially more severe corrosion in metal-based petroleum infrastructure than crude oils due to their higher molecular oxygen content and the presence of various organic acids. To effectively manage such corrosion, it is crucial to understand the corrosion mechanism, particularly the onset of local corrosion, as well as its relationship with the metallic microstructure. Here, using pentanoic acid—a typical degradation product and representative corrosion contributor from biofeedstocks—as the corrosive medium, we capture the real-time initiation and progression in corrosion of carbon steel lamella, which is a model petroleum infrastructure, at nanometer resolution. We correlate in situ liquid-phase transmission electron microscopy imaging of the corrosion process with ex situ characterization of grain size, orientation, and elemental distribution. Through this correlative, multimodal characterization, we identify the key microstructural features that significantly influence corrosion behavior: galvanic corrosion initiates corrosion, strain accelerates corrosion, and lattice orientation guides corrosion propagation. Contrary to aqueous corrosion, corrosion in pentanoic acid is not heavily influenced by the grain boundaries, with similar rates observed in coarse- and fine-grain lamellae. Our observations highlight the importance of intrinsic structural features of carbon steel and their impact on corrosion in biofeedstock-based organic acids, providing insights for potential corrosion mitigation.**

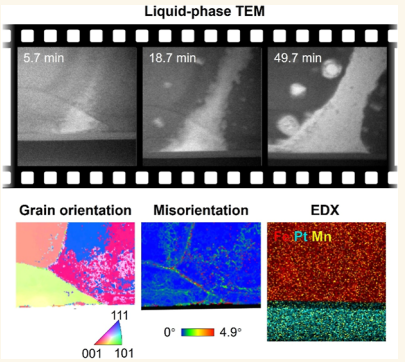

KEYWORDS: *petroleum infrastructure, steel corrosion mechanism, biofeedstock, liquid-phase transmission electron microscopy, microstructure, multimodal characterization*

INTRODUCTION

Corrosion is a global concern that leads to significant financial losses, including in the oil and gas industry, which relies heavily on metal-based infrastructure throughout its supply chain. In petroleum refining alone, the annual direct cost of corrosion had reached $3.7 billion as of 1996.[1] Meanwhile, biofeedstocks, such as triacylglycerol-based biological oils and fats, are regarded as a promising substitute and blend to petroleum due to concerns regarding energy security, renewability, and the carbon cost of the latter.[2] For example, biofuels produced from biofeedstocks can significantly help reduce life-cycle emissions associated with aviation, shipping, and heavy road transport. However, in fully adapting the petroleum infrastructure for biofeedstocks, it remains critical yet greatly underexplored to understand fundamentally their corrosion mechanism and corrosion behaviors. Specifically, compared to crude oils, biofeedstocks can cause even higher cost for corrosion due to their higher molecular oxygen content and the presence of a variety of functional groups, such as esters, carboxylic acid, and ketones, which significantly enhance the corrosivity of the solution.[3] To effectively predict and mitigate corrosion in these aggressive environments, fundamental understandings of corrosion initiation and progression, along with their relation-

Received: April 11, 2025
Revised: July 10, 2025
Accepted: July 11, 2025

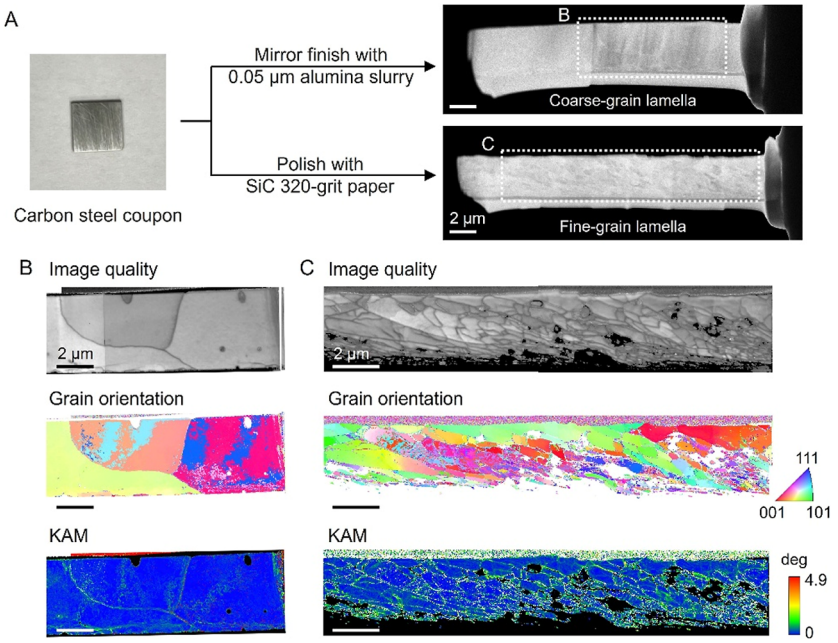

Figure 1. Preparation of carbon steel lamellae with different grain sizes. (A) Different polishing methods to prepare coarse- and fine-grain lamellae from carbon steel coupons. The white boxes highlight the regions characterized in (B,C). (B,C) Structural information on the (B) coarse-grain and (C) fine-grain lamellae, including image quality, grain orientation, and kernel average misorientation (KAM) maps obtained by TKD. Note that in (B,C), multiple partially overlapping images are stitched together to show a large sample region. Scale bars: 2 μm.

ship to microstructural and compositional features of metals, are important.

The corrosion of steel in wet environments is typically governed by two distinct mechanisms: uniform and localized corrosion, where uniform corrosion affects the surface almost evenly and localized corrosion occurs in specific regions of the materials.[4,5] Compared with uniform corrosion, localized corrosion is often more challenging to predict or manage. Localized corrosion contributes majorly to the reduced lifespan of the metal infrastructure used in the oil and gas industry due to its rapid penetration into the steel and subsequent exposure of a larger surface area to the corrosive medium. To understand localized corrosion, it is important to capture the corrosion initiation process, which typically occurs at the atomic or nanometer scale and requires real-time characterization techniques with high spatial resolution. In addition, the metal systems can be complex, involving variations in their microstructures (e.g., grain size and orientation, in-plane strain[6]) and compositions (e.g., existence of carbides,[7] content of chromium[8]), necessitating nanoscale structure and composition mapping to relate the localized corrosion processes to the corresponding local properties. Conventional imaging techniques can face limitations in spatial resolution (e.g., X-ray spectroscopy and optical microscopy), microstructural sensitivity (e.g., atomic force microscopy), or stringent sample requirements (e.g., scanning tunneling microscopy). The recent emergence and advancement of liquid-phase transmission electron microscopy (TEM) provides a powerful tool for imaging nanoscale corrosion processes in real time.[9−14] Pioneering studies have demonstrated the capability of liquid-phase TEM in monitoring the corrosion of carbon steel and stainless steel in aqueous solutions, resolving phenomena like galvanic corrosion at phase interfaces and accompanied cementite ejection.[5,15−17] However, in addition to composition, the influence of structural features, such as strain and lattice orientation, remains underexplored. The behavior of corrosion in organic acids with moderate conductivity, as opposed to in aqueous environments, is particularly relevant to biofeedstocks and remains largely unknown and worth further investigation.

Here, we present the application of liquid-phase TEM to resolve the corrosion initiation and progression in steel immersed in organic acid with nanometer resolution. We focus on pentanoic acid and 1018 carbon steel. Pentanoic acid is a typical example of short-chain organic acids as potential degradation products from triglyceride-based biofeedstocks during refining, with a pK_a close to that of long-chain acids found in biofeedstocks.[18,19] In-depth structural and compositional analysis is provided by integrating in situ imaging with ex situ characterizations of the steel, including transmission Kikuchi diffraction (TKD) for grain size and orientation identification, energy dispersive X-ray spectroscopy (EDX) for elemental distribution, and energy filtered TEM for thickness mapping. With contour tracking and local corrosion rate measurement, we further investigate the correlation between preferred corrosion paths and microstructural features, including strain, lattice orientation, grain boundary (GB), surface curvature, and carbides. We find that, under room temperature, corrosion initiates not only due to galvanic corrosion but also random perforation, with the corrosion front behavior being highly influenced by strain distribution and lattice orientation. GBs, surprisingly, do not exhibit a significant influence on corrosion, which is further supported by a comparison between lamellae with different grain densities. Our experiment provides a mechanistic understanding of the corrosion of carbon steel in organic acids and establishes a multimodal characterization workflow to correlate corrosion with material microstructure and composition, which can potentially provide guidance to long-lifetime

https://doi.org/10.1021/acsnano.5c06142
ACS Nano XXXX, XXX, XXX−XXX

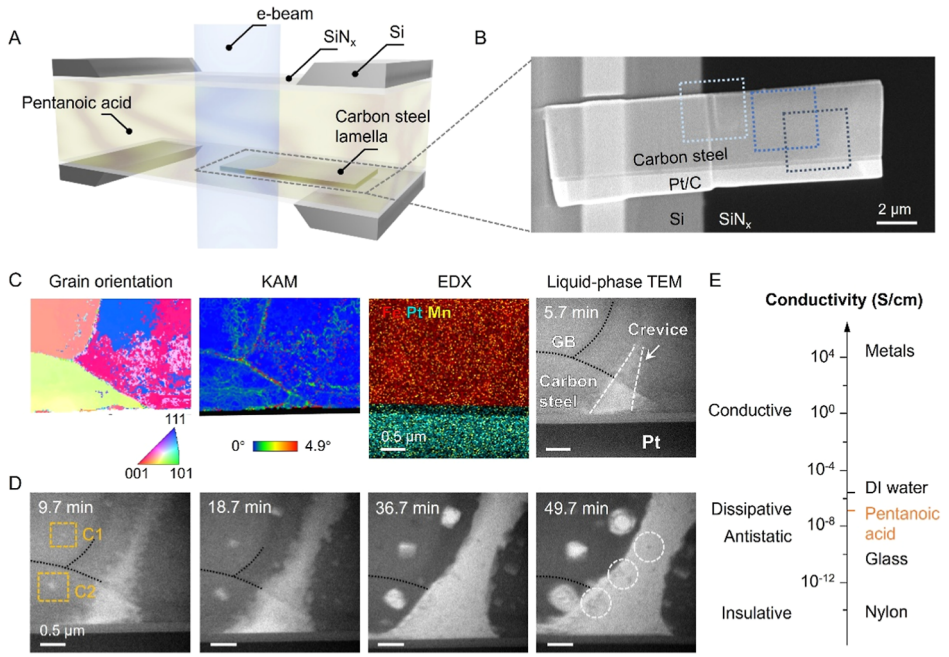

Figure 2. Liquid-phase TEM setup and observation of corrosion initiation. (A) Schematic illustration showing the setup of a liquid-phase TEM, where a carbon steel lamella is positioned parallel to the chip and immersed in pentanoic acid, both sealed between two SiN_x chips. (B) SEM image of the coarse-grain lamella lying on the SiN_x chip. The black box highlights the corrosion initiation area shown in (C,D). The blue and light blue boxes highlight the random perforation areas shown in Figures 4 and 5. (C) Grain orientation (inverse pole figure colored with respect to the *z*-axis orientation), KAM, and EDX maps of the area where corrosion initiates. The white dashed lines in the liquid-phase TEM image label the boundary of the crevice. (D) Time-lapse TEM images showing the corrosion propagation across the lamella. The orange boxes highlight the areas where perforation occurs. The two voids are labeled C1 and C2, respectively. The black dashed lines in (C,D) highlight the GBs. The light gray circles in (D) highlight species that are likely carbonaceous, potentially generated during corrosion. (E) Conductivity of pentanoic acid compared to typical conductivity ranges for different applications. Scale bars: 0.5 μm.

material design for biofeedstock refinement and transportation and to broadly mitigate corrosion of other metallic materials.

RESULTS AND DISCUSSION

Corrosion Initiation and Progression Observed under Liquid-Phase TEM. Carbon steel lamellae with different grain sizes are prepared and characterized to systematically investigate the influence of the microstructure on corrosion behavior (Figure 1). By mirror-polishing the carbon steel coupon with 0.05 μm alumina, we can extract a coarse-grain lamella from it, with three major domains identified inside the lamella based on TKD (Figures 1B and S1). Each domain exhibits a distinct crystallographic orientation to allow comparison of corrosion rates along different directions. To enable clear observation of the corrosion initiation and grain distribution, the thickness of the lamella is controlled at 70−80 nm. Based on TKD results, the grain size within the coarse-grain lamella varies from a few to tens of micrometers, far exceeding the thickness of the lamella. If we assume that the grains extend decently evenly in three dimensions, in the *z* direction, their size can be 2 to 3 orders of magnitude larger than the thickness of the lamella (70−80 nm). Thus, the 2D projection view can reasonably capture the microstructure related to the etching behaviors.

Liquid-phase TEM is further utilized for the nanoscopic imaging of corrosion initiation in the lamella. In the experimental setup, the carbon steel lamella is sealed with the corrosive pentanoic acid medium between two SiN_x chips (Figure 2A). Based on ex situ corrosion tests, the carbon steel coupon corrodes at a rate of 1.31 nm/min in pure pentanoic acid at room temperature, a rate that is also suitable for TEM observation (Table S1). To minimize the influence of the electron beam, instead of movies, we take images every one min with an exposure time of 1.0 s and a low dose rate of 1.25 e^{-} $Å^{-2}$ s^{-1}.

Based on the scanning electron microscopy (SEM) image (Figure 2B), two distinct layers can be observed in the lamella, both deposited during the standard focused ion beam (FIB) extraction process: a layer primarily composed of amorphous Pt deposited using e-beam, in physical contact with carbon steel, and a layer of ion beam-deposited Pt. As shown in Figure 2C,D and Video S1, corrosion is triggered at the interface of the amorphous Pt layer and ferrite, which can be attributed to galvanic corrosion. With Pt serving as the cathode and ferrite as the anode, a nanoscale battery is formed and can accelerate the dissolution of the anodic ferrite (more discussions on the role of Pt are in the Supporting Information). Meanwhile, the conductivity of pentanoic acid is measured to be 0.27 μS/cm (Table S2 and Figure 2E), falling in the range between conductive and insulative solvents.[20] The associated high resistance in the solvent leads to a drop-off in galvanic corrosion rates as distance between the anode and cathode increases and thus the formation of a crevice between the Pt layer and ferrite at the initial step of the corrosion (schematic illustration provided in Figure S2).[21]

Interestingly, instead of expanding along the Pt layer, the corrosion propagates across the lamella, forming a crevice perpendicular to the Pt surface (Figure 2D). EDX mapping suggests no carbide in the viewing area, ruling out the possibility of carbide-induced galvanic corrosion. By comparing side-by-side the liquid-phase TEM image, grain orientation,

https://doi.org/10.1021/acsnano.5c06142
ACS Nano XXXX, XXX, XXX−XXX

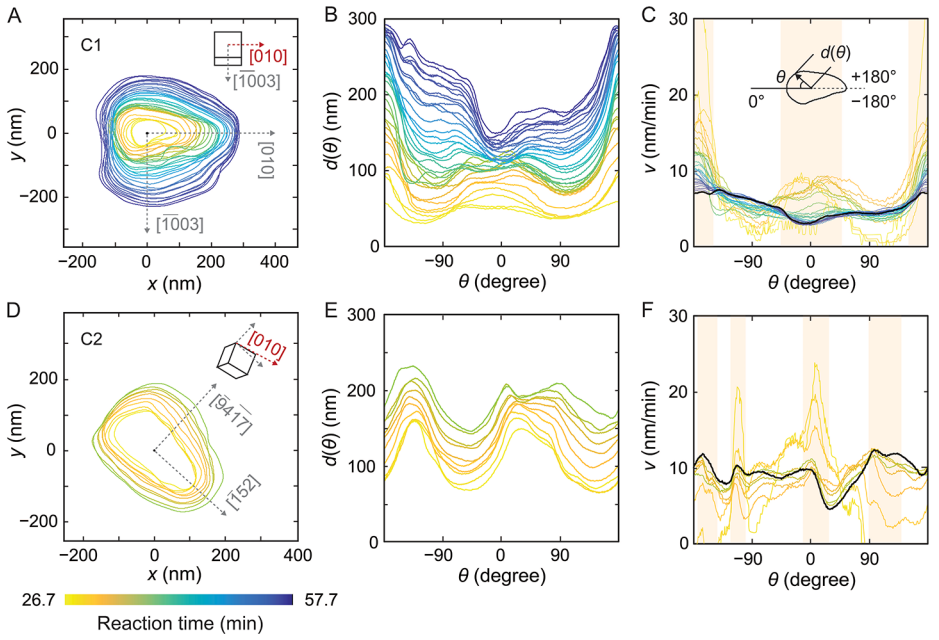

Figure 3. Anisotropic growth of voids and dependence on lattice orientation. (A,D) Contour plots of (A) C1 and (D) C2 voids highlighted with orange boxes in Figure 2D. The insets show the grain orientation (red) and corrosion (gray) direction. (B,E) Shape fingerprints of (B) C1 and (E) C2 voids showing their expansion and shape evolution during corrosion. (C,F) Local corrosion rates as a function of θ for (C) C1 and (F) C2 voids. The thick black lines represent the final corrosion rate over all directions. The orange shadows highlight the directions with faster corrosion rates. The same color bar for reaction time applies to (A–F).

and KAM maps obtained from TKD (Figures 2C and S3), we find that the crevice is located in the region with large local misorientation, which also serves as an indicator of strain in this area. Note that the KAM map captures misorientations not only at GBs but also between different domains within a single grain, enabling the assessment of local strain across the lamella (Methods). While it qualitatively shows the local misorientations, the specific misorientation values can be sensitive to kernel parameters such as neighborhood definition.[22] Besides local misorientation, the thickness map derived from energy loss of electrons passing through the sample also shows vertical stripes across the lamella (Figure S4), providing additional evidence to the existence of vertically distributed strain area.[23] The presence of strain may lead to larger bond length, either in-plane or out-of-plane, and thus accelerate the dissolution of atoms.[24] The well-aligned strain distribution and corrosion propagation direction suggest that strain can significantly accelerate the corrosion of carbon steel, exerting an influence that may surpass that of galvanic corrosion when pentanoic acid is used as the solvent.

It should be noted that though a GB is present perpendicular to the crevice, surprisingly, no apparent corrosion acceleration is observed along this GB, as evidenced by the absence of "branch" protruding from the crevice (Figure 2D). GBs can be briefly categorized into two types: low-angle GBs (typically with a grain-to-grain misorientation angle <15°) and high-angle GBs (>15°), with the latter expected to be more susceptible to corrosion.[25,26] In practice, the energy of GBs and their contribution to corrosion are more complex. Each GB has its own sensitivity to corrosion, whose energy can be affected by five-dimensional parameters, including three for the GB misorientation and two for the plane inclination.[27] For example, in austenitic stainless steels, twin boundaries might be more corrosion-resistant than other high-angle GBs due to their highly regular and coherent atomic structure.[28] Besides, GBs are also often associated with localized strain, which can significantly affect corrosion. Even slight prestrain annealing has been shown to improve resistance to intergranular corrosion effectively.[29] In our work, the observation of no obvious corrosion acceleration at GBs may be attributed to favorable atomic structures and strain distributions at these specific sites that we observe, where further thorough investigations involving atomic-resolution imaging and local strain mapping of more GBs will be critical for understanding their correlation. Moreover, EDX analysis of the lamella shows no accumulation of carbon or gallium at the GBs, suggesting that impurity segregation is likely not a contributing factor (Figure S4). This absence of corrosion acceleration is further supported by comparable corrosion rates in both coarse- and fine-grain lamellae, which will be detailed later.

Anisotropic Growth of Voids and Corrosion Preferred along the ⟨100⟩ Direction. Aside from the crevice propagation, we also observe random perforations on the lamella, highlighted by the orange boxes in Figure 2D. Instead of growing into a circular shape, these voids adopt elliptical or even rectangular shapes (Figure 3A,D), suggesting anisotropic corrosion at the nanoscale. To better characterize their shape evolution, we analyze the shape of the voids, using a fingerprint function defined as the length $d(\theta)$ of the distance vector with orientation θ connecting a point on the shape contour to the centroid of the contour as a function of θ.[30] For the C1 void shown in Figure 3B, two peaks gradually emerge at approximately 0° and 180°, which later split into four peaks at −150°, −60°, 60°, and 180°, indicating an evolution from an ellipse to a polygonal shape resembling a rectangle.

Directional corrosion is revealed by calculating the local corrosion rates v, defined as $d(\theta, t) - d(\theta, t_0)$ divided by the reaction time from the start of tracking to the specific time point of interest ($t - t_0$, details can be found in Methods). At the early stages of corrosion, local corrosion rates in the

https://doi.org/10.1021/acsnano.5c06142
ACS Nano XXXX, XXX, XXX−XXX

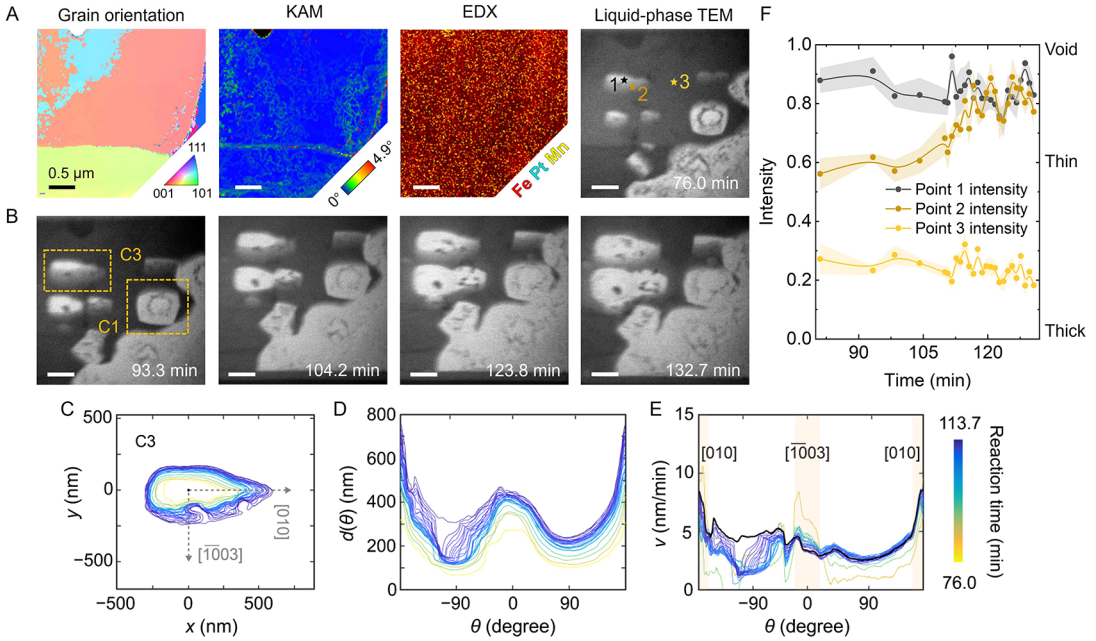

Figure 4. Corrosion acceleration along the ⟨100⟩ direction observed in other regions. (A) Grain orientation, KAM, and EDX maps of the area highlighted with a blue box in Figure 2B, where more perforations are observed. (B) Time-lapse liquid-phase TEM images showing the growth of the voids into elliptical shapes. (C) Contour plot, (D) shape fingerprint, and (E) local corrosion rate of the C3 void highlighted by an orange box in (B). (F) Intensity changes of three positions of interest labeled in (A) during corrosion. A low intensity suggests the existence of a thick lamella, while the increase in intensity suggests its corrosion into a thinner layer and finally a void. Scale bars: 0.5 μm.

horizontal directions ($\theta = 0°$ and 180°) are significantly higher than those in other directions (Figure 3C). As the reaction proceeds, the corrosion rate at $\theta = 0°$ is gradually surpassed by those at $\theta = \pm 90°$. If we plot the corrosion rates in four key directions associated with the formation of a rectangular void ($\theta = 0°$, 180°, and ±90°), a transition can be observed at around 38.7 min when the local corrosion rates at $\theta = \pm 90°$ exceed that of $\theta = 0°$ (Figure S5). The transition might be related to in-plane strain and its release during corrosion, considering the crevice expansion and appearance of more perforations around the C1 void at the same time.

Overlaying the liquid-phase TEM images with the grain orientation map reveals that the $\theta = 180°$ direction aligns with the [010] direction of *bcc* ferrite, while the $\theta = -90°$ direction corresponds to the $[\bar{1}003]$ direction, close to the projection of the $[\bar{1}00]$ direction on the lamella plane. Combining these observations, it appears that corrosion tends to be preferred along the ⟨100⟩ direction. Such preference can be largely attributed to the lower packing density of atoms on {100} facets of *bcc* ferrite (Figure S6), which results in a higher surface energy and increased vulnerability to corrosion.[31] Additionally, faster hydrogen evolution on {100} facets of ferrite, which serves as the cathodic reaction balancing iron oxidation, may also contribute to this preference.[32−34] It should be noted that such corrosion acceleration along ⟨100⟩ directions has also been reported in bulk corrosion tests in aqueous solutions, where {100} planes are identified as the most susceptible to cracking and pit propagation compared to other low index facets, showing consistency with our observations.[6]

The corrosion acceleration along the ⟨100⟩ direction is also evident in many other voids. For example, the growth of the C2 void, located in a different grain with a distinct orientation, shows a preference toward the $\theta = -135.3$ and 146.1° directions (Figure 3D−F), corresponding to the $[\bar{1}52]$ and $[\bar{9}4\bar{1}7]$ directions of ferrite. These two directions are close to the projections of the [010] and $[00\bar{1}]$ directions on the lamella plane. For the C3 void located in the same grain as C1, it grows into an elliptical shape, like the other two voids under it (Figure 4A,B and Video S2). The faster expansion along the $\theta = 180°$ direction indicates a faster corrosion rate toward the [010] direction (Figure 4C−E), consistent with our observation in the C1 void. This recurring preference observed in grains with different orientations provides strong evidence for the accelerated corrosion along the ⟨100⟩ direction in pentanoic acid. Moreover, these voids gradually evolve from elliptical shapes (76.0 min, Figure 4) into more polygonal shapes, resembling rectangles or their overlap given the merging of voids (141.2 min, Figure S7). The alignment of the longer axes of these voids with the ⟨100⟩ direction of *bcc* ferrite further supports the facet dependence on corrosion rates.

Closer inspection of the void boundaries shows that some edges do not appear to be perpendicular to the substrate. If we plot the TEM image intensity at a point on the bottom edge of the C3 void, we observe an increase in intensity as the reaction proceeds, suggesting a gradual decrease in thickness at this point and an angle existing between the corrosion front plane with the SiN_x substrate (Figure 4F). In terms of lattice orientation, the $\theta = -90°$ direction aligns with the $[\bar{1}003]$ direction in *bcc* ferrite, leaving an angle of $\theta = 16.7°$ with the $[\bar{1}00]$ direction. Consequently, for corrosion that prefers the $[\bar{1}00]$ direction, its front plane will not be perpendicular to the substrate.

Additionally, aside from localized corrosion, uniform corrosion may also exist, gradually thinning the lamella and leading to its increasing contrast during imaging.[4] One piece of evidence is the formation of ferrite thin layers as corrosion progresses, which are observed in multiple regions of the lamella (Figures 2D and 5). Notably, the lack of accelerated

https://doi.org/10.1021/acsnano.5c06142
ACS Nano XXXX, XXX, XXX−XXX

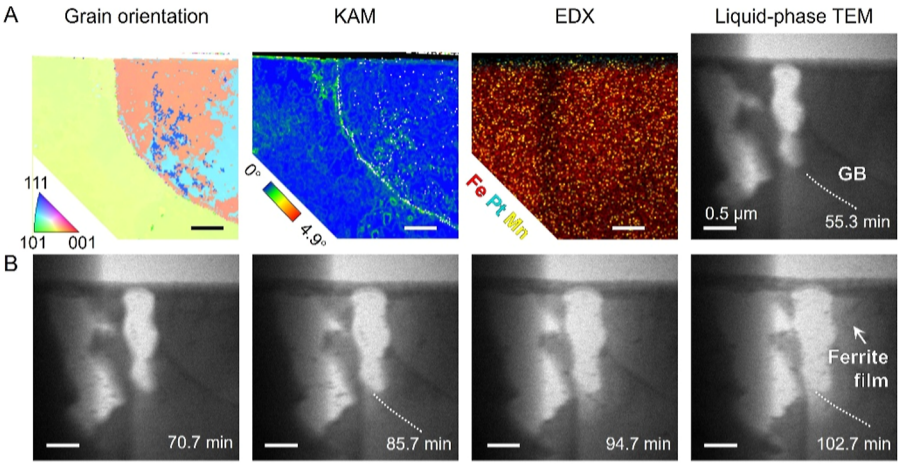

Figure 5. Corrosion near bent area of lamella and observation of lamella thinning. (A) Grain orientation, KAM, and EDX maps of the area highlighted with a light blue box in Figure 2B. (B) Time-lapse TEM images showing corrosion progression near the bent area. The white dashed curves indicate the GB. Starting from around 85.7 min, a continuous increase in contrast across the lamella is observed, suggesting the potential presence of uniform corrosion. Scale bars: 0.5 μm.

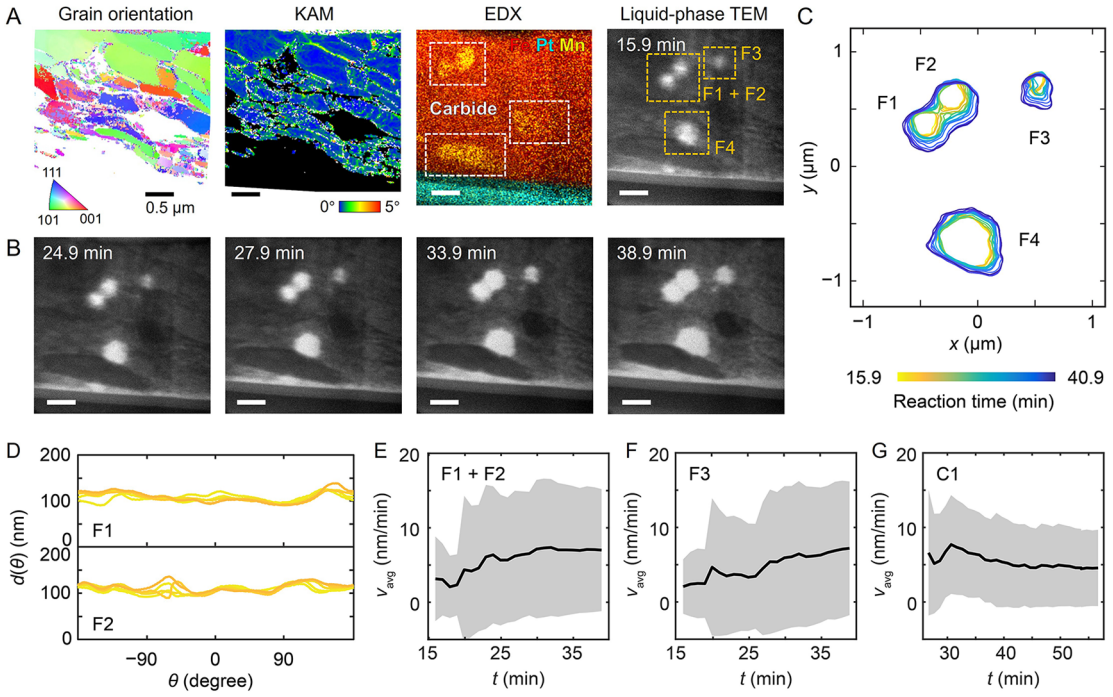

Figure 6. Corrosion in fine-grain lamella and influence of grain density. (A) Grain orientation, KAM, and EDX maps of the region where corrosion is initiated near the carbides and Pt layer. The white boxes in the EDX map highlight the locations of carbides. The orange boxes in the TEM image label the positions of voids. (B) Time-lapse TEM images showing the growth of voids in the fine-grain lamella. (C) Contour plot of the voids labeled in (A). (D) Shape fingerprints of the F1 and F2 voids showing their circular shape before merging with each other. (E–G) Averaged local corrosion rates of (E) the F1 and F2 voids and (F) the F3 void in the fine-grain lamella, compared to (G) that of the C1 void in the coarse-grain lamella. The shadow shows the standard deviation of local corrosion rates. Scale bars: 0.5 μm.

corrosion along the GB is also observed in Figure 5B, an area closer to the bend, further supporting our observation that GBs do not serve as preferred pathways for corrosion propagation in pentanoic acid.

Corrosion Rate Comparison between Coarse- and Fine-Grain Lamella. In applications, manufacturing processes such as bending or polishing can cause grains to break into smaller pieces.[35] To investigate the influence of the size and density of grains on corrosion rates, we polish the carbon steel coupon with SiC 320-grit paper and prepare a lamella enriched with fine grains, typically less than 1 μm in diameter (Figure 1C). The dense, smaller grains inside the lamella, compared to the coarse-grain one, can be clearly resolved by both TKD and high-angle annular dark-field scanning TEM (HAADF-STEM), as shown in Figures 6A and S8. The fine-grain lamella contains multiple carbides. Thus, along with the gap near the Pt/C layer, we also observe perforations occurring near the carbides, potentially due to galvanic corrosion (Figure 6B and Video S3). The corrosion of carbides is significantly slower than that of ferrite. In the later stage of corrosion, when most of the ferrite has dissolved, carbides remain visible and largely

https://doi.org/10.1021/acsnano.5c06142
ACS Nano XXXX, XXX, XXX−XXX

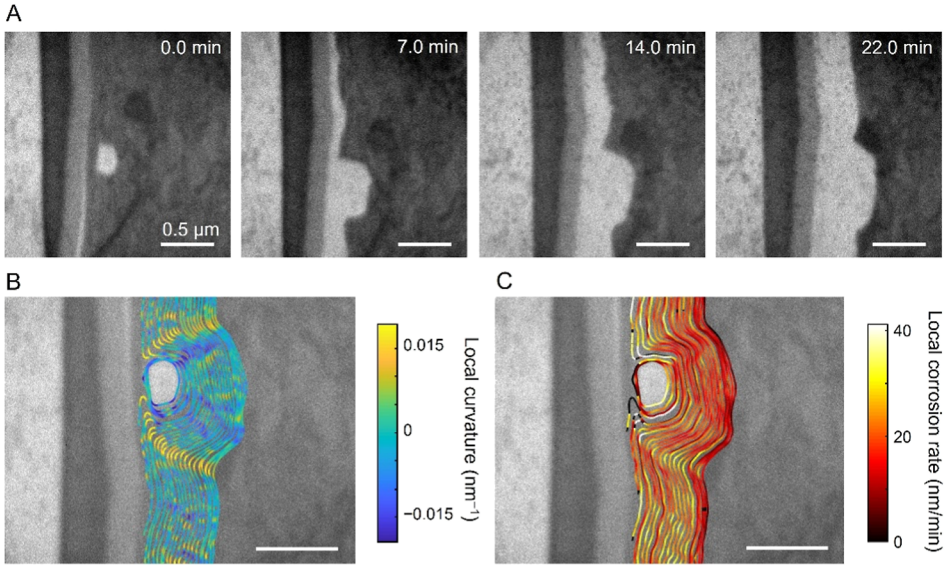

Figure 7. Faster corrosion on convex surface. (A) Time-lapse TEM images showing the corrosion progression in another fine-grain lamella immersed in pentanoic acid at room temperature. The first image was set as 0 min. (B,C) Contours of void/crevice colored to its (B) local surface curvatures and (C) local corrosion rates. Scale bars: 0.5 μm.

uncorroded, consistent with their role as the cathode during galvanic corrosion (Figure S9).

Different from the elliptical or rectangular voids observed in the coarse-grain lamella, the voids in the fine-grain lamella mostly grow into circular shapes. This suggests a loss of faster corrosion along specific directions due to the surrounding grains with varying orientations (Figure 6C). The circular shape of these voids can be further captured by the flat curves in their shape fingerprints, with examples from voids F1 and F2 shown in Figure 6D. When two voids merge, protrusions are formed in the merging area, accompanied by faster corrosion in these regions (Figure S10). Such correlation between surface convexity and corrosion acceleration is also evident in another fine-grain lamella, whose boundaries are more distinct to observe (Figure 7 and Video S4). Protrusions are often associated with low-coordinated atoms and the presence of strain, both of which can contribute to an acceleration in corrosion.[24]

If we compare the average local corrosion rates of voids in coarse- and fine-grain lamellae, a similar corrosion rate around 5 nm/min is observed in both of them (Figures 6E−G and S11, and detailed values can be found in Table S3). This similarity provides further support to our prior observation that GBs do not significantly accelerate the corrosion of carbon steel in pentanoic acid. The slightly accelerated corrosion in the fine-grain lamella could be related to the different corrosion rates in fine grains with different orientations, which may lead to rougher void boundaries and potential detachment of small grains. Notably, the average corrosion rate of 5 nm/min, as measured from in situ imaging of void expansion, is close to that measured from bulk corrosion tests (1.3 nm/min), suggesting a minimum influence from the electron beam. The slightly faster corrosion in the lamella may be attributed to galvanic corrosion induced by the Pt layer deposited during FIB preparation and the fact that the lamella for the TEM experiment has a much smaller thickness than the bulk samples. Specifically, the calculation of corrosion rate is normalized by surface area to account for the possible contribution of a thinned lamella sample compared with bulk steel. As the thickness decreases from micrometers in the metal coupon (plane strain-like condition) to nanometers in the lamella (plane stress-like condition), potential relaxation of surface strain/stress in the lamella may also contribute to its faster corrosion rate observed.[36] Future experiments may consider using a nonconductive protective layer during FIB preparation,[37,38] as well as reaction conditions closer to real-world environments, such as elevated temperatures and more complex corrosive media.[3]

While the major chemical reaction is oxidation of Fe:[39]

$$2C_4H_9COOH + Fe \rightarrow (C_4H_9COO)_2Fe + H_2$$

the presence of an electron beam may lead to radiolysis of the solvent, generating radicals and acids with varying molecular weights.[40,41] On one hand, corrosion acceleration by radicals and short-chain acids contradicts its deceleration by long-chain acids or alcohols generated from the combination of radicals. This necessitates further analysis of the radiolysis products and their relative concentrations. On the other hand, the comparable corrosion rates in our liquid-phase TEM and bulk corrosion tests, the formation of voids and deposits on the carbon steel coupon after the bulk corrosion test, and the initiation of corrosion in different areas of the lamella all suggest that the corrosion observed in the lamella is majorly driven by the chemical reactions generic in the solution, with minimal influence from the electron beam (Figure S12, more discussions on beam effect in the Supporting Information).

CONCLUSIONS

Using liquid-phase TEM, we track the nanoscale corrosion initiation in carbon steel lamella immersed in pentanoic acid, which is a typical degradation product of triglyceride-based biofeedstocks. The real-time imaging, combined with grain orientation mapping from TKD and elemental mapping from EDX, allows us to correlate the structural features of carbon steel to the corrosion behavior. Our observations highlight three key features influencing corrosion behavior (Table 1): (i) strain that can significantly accelerate corrosion, whose impact on corrosion propagation may even surpass galvanic corrosion

https://doi.org/10.1021/acsnano.5c06142
ACS Nano XXXX, XXX, XXX−XXX

Table 1. Structural Features and Their Influence on Carbon Steel Corrosion in Pentanoic Acid

structural feature	corrosion path	observation
strain/local misorientation	faster corrosion in the area with larger strain/local misorientation	Figure 2
lattice orientation	faster corrosion along the ⟨100⟩ direction	Figures 3 and 4
carbide	inducing galvanic corrosion to promote corrosion initiation	Figure 6
GB	no obvious influence on corrosion rate	Figures 2 and 6
surface curvature	faster corrosion on convex surface	Figures 7 and S10

in pentanoic acid; (ii) lattice orientation, where faster corrosion is observed along the ⟨100⟩ direction in *bcc* ferrite, indicating a directional preference induced by the atomic packing on specific lattice planes; and (iii) GB, which surprisingly shows minimal influence on the corrosion rate, challenging the conventional assumption of their contribution to corrosion acceleration. Besides, the occurrence of perforations on the lamella is also worth special attention, as it often acts as an initiator for localized corrosion. These perforations can be triggered by galvanic corrosion (in the presence of carbides or other cathodic elements), and their further expansion can be strongly influenced by the strain distribution, lattice orientation, and surface curvatures.

These nanoscale structural insights provide us with valuable guidance for material design toward an enhanced lifespan of pipelines, refineries, and other infrastructures. For example, given the significant influence of strain on corrosion propagation, thermal or mechanical treatments (e.g., annealing and tempering) can be employed to reduce unnecessary strain inside carbon steel, suppressing directional and rapid corrosion progression.[42,43] Regarding the accelerated corrosion along certain crystallographic directions, as well as the occurrence of random perforations, the surface coating has been widely adopted as an effective protection method. These coatings include passivation layers (e.g., aluminum oxide) that protect the surface from contacting corrosive media[44] and sacrificial anodes (e.g., zinc) that corrode more preferentially than steel.[45] Elemental doping can also alter the microstructure and composition of steel, improving its corrosion resistance. For example, Nb doping has been shown to refine grain structure and promote the exposure of {110}-oriented grains, while Nb-deficient steel tends to exhibit irregular microstructures with a mixture of fine and coarse grains.[46] Note that the role of elemental doping may vary depending on the steel type and reaction conditions, including corrosive medium and temperature, and system-specific analyses are required. Regarding GBs, although they do not show a direct influence in our study, their role in corrosion acceleration is still under debate. This complexity arises from the dependence on GB types, specific atomic arrangements, and localized strain distributions. Under certain conditions, GBs may even facilitate rapid formation of a surface passivation layer, protecting the underlying infrastructure from fast corrosion.[47] Further research is needed to fully understand their impact under different reaction conditions.

METHODS

Lamellae Preparation and Transfer to SiN_x Chip. The carbon steel coupons (CS1018, ca. 4.52 × 4.49 × 0.44 mm) were received from bp and used for the extraction of lamellae. The chemical composition was provided in Table S4. To prepare coarse-grained lamella, the coupon was mirror polished with a 0.05 μm alumina slurry. For fine-grained lamella, the coupon was polished with SiC 320-grit paper at a speed of 100 rpm and 1 min for each side, using Buehler MetaServ 250. A continuous flow of water was used to prevent heating. After being polished, the coupons were sonicated in isopropyl alcohol for 5 min to clean the surface.

The polished coupon was then affixed to an SEM stub for the following extraction of lamella using FIB (Thermo Scientific Scios 2 DualBeam). A 0.5 μm-thick protective layer of Pt was first deposited onto a (18−20) × 2 μm area of the coupon surface with a 2 kV electron beam (1.6 nA current), followed by deposition of another 1.5 μm-thick Pt layer with a 30 kV Ga ion beam. Trench cut was performed at 30 kV with a 15 nA Ga beam. An EasyLift micromanipulator was used to lift the lamella and attach it to a Cu TEM lift-out grid. The lamella was further thinned to ca. 70 nm, followed by a final 2 kV Ga ion thinning step to remove the Ga-ion-damaged surface layer. Before transferring to the SiN_x chip, the lamella was characterized in terms of grain size and orientation, elemental distribution, and thickness, which is detailed in the following section.

For in situ corrosion tests, the lamella was removed from the TEM grid and transferred to a SiN_x chip (30 μm × 650 μm with 50 nm thick SiN_x window, Hummingbird Scientific). Specifically, the lamella was removed from the TEM grid using the FIB lift-out technique with 16 kV Ga ion beam cuts and then transferred to the edge of the SiN_x window. The lamella was not exposed to live imaging for both electron and ion beams, and the lowest Ga-ion current (10 pA) was used to minimize Ga-ion damage. The lamella rested partially on the thick Si edge and partially on the window. An e-beam Pt layer of 150 nm thick was deposited onto the bottom of the lamella at 2 kV, sticking the lamella to the Si substrate. Then, a 30 kV, 0.1 nA Ga ion beam was used to cut the lamella from the needle while ensuring that the SiN_x window and the part of the lamella over the window were not exposed to the beam.

Characterization of the Lamella Structure and Composition. TKD mapping of the carbon steel lamella was performed on a Thermo Scios2 Dual-Beam SEM/FIB. The TKD patterns were captured using an accelerating voltage of 30 kV, a probe current of 6.4−13 nA, and a step size of 20 nm (TEAM software, EDAX Inc.). Data analysis, including image quality, grain orientation, and KAM mapping, was performed by using the OIM Data Analysis 8 (EDAX Inc.) software. Specifically, in the KAM map, the average misorientations between each pixel and the six pixels surrounding it were calculated and assigned to the center pixel, allowing the resolution of both GBs and local misorientations between different domains within each grain. A one-pixel neighborhood and a default misorientation range of 0−5° were used in this work to better highlight the distribution of local misorientations, particularly those with small angles.

EDX mapping was performed on a ThermoFisher Talos F200X G2 S/TEM at 200 kV. The total acquisition time was 20 min, and the beam current was 17 pA. SEM−EDX mapping was performed on a Hitachi S-4800 SEM equipped with Oxford's Ultim Max detector at 20 kV, with a probe current of 10 μA for ∼10 min. The sample thickness was measured using the thickness mapping function of a Hitachi H-9500 Dynamic Environmental TEM instrument at 300 kV.

Liquid-Phase TEM Imaging. Liquid-phase TEM imaging was performed on a Hitachi 9500 TEM with a LaB_6 emitter at 200 kV, and a spot size of Micro 1 was used for TEM imaging. Images in Figures 2 and 4−6 were captured by a Gatan Orius fiberoptically coupled CCD camera with an exposure time of 1.0 s every one min with a dose rate of 1.25 $e^- Å^{-2} s^{-1}$. Images in Figure 7 were captured with an exposure time of 2.0 s every one min with a dose rate of 0.9 $e^- Å^{-2} s^{-1}$. The beam was blocked in the interval. A liquid flow TEM holder (Hummingbird Scientific) was used. In a standard protocol, ∼ 0.5 μL of pentanoic acid was dropped onto a SiN_x spacer chip (window: 50 μm × 200 μm × 50 nm, 250 nm spacer, Hummingbird Scientific) and overlaid with a window chip (window: 30 μm × 650 μm × 50 nm, Hummingbird Scientific) where the lamella was placed on. The spacer

https://doi.org/10.1021/acsnano.5c06142
ACS Nano XXXX, XXX, XXX−XXX

chip was pretreated with oxygen plasma (Harrick Plasma Cleaner PDC23G) at a low radio frequency level for 27 s to clean their surface. The window chip was not plasma cleaned to avoid the oxidation of the lamella. After the experiment, the chips were disassembled, and the window chip was immersed in ethanol for ∼2 min, rinsed with ethanol twice, and then left to dry.

Contour and Corrosion Rate Analysis. The time-lapse liquid-phase TEM images in DM4 format with a 2048 pixel × 2048 pixel resolution were exported into TIFF format with the same contrast and brightness settings, as well as minimum compression. They were aligned using sped-up robust features, which detected interest points in the successive frames and then computed the geometric transformations from the matching point pairs. For data sets in Figure 3, manual alignment was performed before running the alignment script to elevate the algorithm performance. All further analyses, including contour tracking and overlaying, local corrosion rate, and local average corrosion rate analysis, are based on the aligned TEM images. After alignment, contour tracking for each data set was performed by adaptive pixel intensity thresholding and boundary detection. The shape fingerprints $d(\theta)$ were computed for all selected contours following previous publication with optimizations.[30] Vectors with angles θ covering −179° to 180° were generated at an interval of 1°, spreading out from the geometrical centroid of the contour at the first recorded frame of the analyzed time interval. The length $d(\theta)$ was calculated as the sum of the distances traveled by each angle vector within the void contour. As most of the voids are convex, this method produces the centroid-to-contour distance and highlights the elliptical or rectangular shape by showing peaks at certain angles. For some voids that merged as corrosion proceeded, this method describes the contour as well as the concaveness that highlights the angle of the merging area.

The local corrosion rates v in Figures 3 and 4 were calculated as a function of angle θ and time t following

$$v(\theta, t) = \frac{d(\theta, t) - d(\theta, t_0)}{t - t_0} \quad (1)$$

where t_0 is the time of the first recorded frame of the analyzed time interval. This local corrosion rate extracts the geometrical and directional features in the local corrosion process, which is later correlated to the local lattice orientation. While most of the local corrosion rate $v(\theta,t)$ is larger than 0, due to the error in alignment and tracking, $v(\theta,t)$ can be smaller than 0 when the local corrosion rate is low at the beginning of corrosion.

The average corrosion rates $v_{avg}(t)$ in Figures 6, 7, S10, and S11 were calculated by using a different method to minimize the influence of concaveness and merging of two voids. We first computed the local center of curvature P_c and local curvature of each point P on the void contour at the previous time point t by fitting a circle using the Pratt method.[48] To find the corresponding points on the next time point t', we find the nearest intersection between the vector $\overrightarrow{PP_c}$ and the void contour at t' as Q. The local distance between the two contours at t is calculated as $\|P - Q\|$ and $v_{avg}(t)$is calculated as follows:

$$v_{avg}(t) = \frac{1}{N(t' - t)} \sum_{i=1}^{N} \|P_i - Q_i\| \quad (2)$$

where N is the total number of points on the void contour at t. The intensity change analysis in Figure 4 was tracked by selecting pixels of interest and calculating the average intensity of eight neighbors around the pixels and themselves to avoid extreme values from noise. All analyses were performed using customized MATLAB scripts.

ASSOCIATED CONTENT

Supporting Information

The Supporting Information is available free of charge at https://pubs.acs.org/doi/10.1021/acsnano.5c06142.

Procedure for lamella preparation and transfer, EDX, TEM, and thickness maps of the coarse- and fine-grain lamellae, schematic illustration of galvanic corrosion mechanism, EDX of liquid chip after corrosion, corrosion rates at different directions for C1, crystal structure of *bcc* ferrite, TEM images of lamellae and coupon after corrosion, curvature and local etching rate analysis for F1 and F2, and average local corrosion rates for voids in coarse-grain lamella (PDF)

Liquid-phase TEM imaging (left) and corresponding contour tracking of C1 and C2 (right) showing the perforation in the coarse-grain lamella and subsequent growth of the voids into elliptical shapes. Dose rate: 1.25 $e^-/(Å^2 \cdot s)$ (MP4)

Liquid-phase TEM imaging (left) and corresponding contour tracking of C3 (right) showing the perforation in the coarse-grain lamella and subsequent growth of the void into an elliptical shape. Dose rate: 1.25 $e^-/(Å^2 \cdot s)$ (MP4)

Liquid-phase TEM imaging (left) and corresponding contour tracking of F1−F3 (right) showing the perforation in the fine-grain lamella, subsequent growth of voids into circular shapes, and merging of voids (F1 and F2). Dose rate: 1.25 $e^-/(Å^2 \cdot s)$ (MP4)

Liquid-phase TEM imaging (left) and corresponding contour tracking of the corrosion front (right) showing the formation and expansion of a void and crevice in another fine-grain lamella, along with accelerated corrosion observed on the convex surface. Dose rate: 0.9 $e^-/(Å^2 \cdot s)$ (MP4)

AUTHOR INFORMATION

Corresponding Author

Qian Chen − *Department of Materials Science and Engineering, Grainger College of Engineering, University of Illinois Urbana—Champaign, Urbana, Illinois 61801, United States; Materials Research Laboratory, Grainger College of Engineering and Beckman Institute for Advanced Science and Technology, University of Illinois Urbana—Champaign, Urbana, Illinois 61801, United States; Department of Chemistry, University of Illinois Urbana−Champaign, Urbana, Illinois 61801, United States;* orcid.org/0000-0002-1968-441X; Email: qchen20@illinois.edu

Authors

Zhiheng Lyu − *Department of Materials Science and Engineering, Grainger College of Engineering, University of Illinois Urbana—Champaign, Urbana, Illinois 61801, United States; Materials Research Laboratory, Grainger College of Engineering, University of Illinois Urbana—Champaign, Urbana, Illinois 61801, United States;* orcid.org/0000-0002-1343-4057

Samyukta Shrivastav − *Department of Materials Science and Engineering, Grainger College of Engineering, University of Illinois Urbana—Champaign, Urbana, Illinois 61801, United States*

Jiahui Li − *Department of Materials Science and Engineering, Grainger College of Engineering, University of Illinois Urbana—Champaign, Urbana, Illinois 61801, United States;* orcid.org/0000-0001-9100-6579

Chang Qian − *Department of Materials Science and Engineering, Grainger College of Engineering, University of Illinois Urbana—Champaign, Urbana, Illinois 61801, United States*

https://doi.org/10.1021/acsnano.5c06142
ACS Nano XXXX, XXX, XXX−XXX

Lehan Yao − *Department of Materials Science and Engineering, Grainger College of Engineering, University of Illinois Urbana—Champaign, Urbana, Illinois 61801, United States;* orcid.org/0000-0003-1945-833X
Nachi Shah − *Department of Materials Science and Engineering, Grainger College of Engineering, University of Illinois Urbana—Champaign, Urbana, Illinois 61801, United States*
Maryam Eslami − *Illinois Applied Research Institute, University of Illinois Urbana—Champaign, Urbana, Illinois 61801, United States*
Chang Liu − *Department of Materials Science and Engineering, Grainger College of Engineering, University of Illinois Urbana—Champaign, Urbana, Illinois 61801, United States;* orcid.org/0000-0001-8091-7940
Sheila Ismail − *BP Technology, Chicago, Illinois 60606, United States*
John Shabaker − *BP Technology, Chicago, Illinois 60606, United States*
Eric Doskocil − *BP Technology, Chicago, Illinois 60606, United States*
Daniel V. Krogstad − *Department of Materials Science and Engineering, Grainger College of Engineering, University of Illinois Urbana—Champaign, Urbana, Illinois 61801, United States; Illinois Applied Research Institute, University of Illinois Urbana—Champaign, Urbana, Illinois 61801, United States;* orcid.org/0000-0001-9953-1378
Jessica A. Krogstad − *Department of Materials Science and Engineering, Grainger College of Engineering, University of Illinois Urbana—Champaign, Urbana, Illinois 61801, United States; Materials Research Laboratory, Grainger College of Engineering, University of Illinois Urbana—Champaign, Urbana, Illinois 61801, United States;* orcid.org/0000-0003-0628-0501

Complete contact information is available at: https://pubs.acs.org/10.1021/acsnano.5c06142

Notes

The authors declare no competing financial interest.

ACKNOWLEDGMENTS

The authors would like to acknowledge the funding and technical support from bp through the bp International Centre for Advanced Materials (bp-ICAM). Experiments were carried out in the Materials Research Laboratory (MRL) Central Research Facilities, University of Illinois.

REFERENCES

(1) Koch, G. H.; Brongers, M. P.; Thompson, N. G.; Virmani, Y. P.; Payer, J. H. *Corrosion Cost and Preventive Strategies in the United States*; Federal Highway Administration, 2002.
(2) Marker, T. L. *Opportunites for Biorenewables in Oil Refineries UOP*; LLC, 2005.
(3) Liu, D.; Shrivastav, S.; Daraydel, S.; Levandovsky, N.; An, H. Y. S.; Shevade, S.; Chen, Q.; Krogstad, J. A.; Krogstad, D. V. Biofeedstock-Induced Metal Corrosion: Reactions Between Carbon Steel and Triacylglycerol-Based Solutions at Elevated Temperature. *Corros. Sci.* **2023**, *216*, 111088.
(4) Callister, Jr. W. D.; Rethwisch, D. G. *Fundamentals of Materials Science and Engineering: An Integrated Approach*, 5 ed.; John Wiley & Sons: NJ, United States, 2018.
(5) Hayden, S. C.; Chisholm, C.; Grudt, R. O.; Aguiar, J. A.; Mook, W. M.; Kotula, P. G.; Pilyugina, T. S.; Bufford, D. C.; Hattar, K.; Kucharski, T. J.; Taie, I. M.; Ostraat, M. L.; Jungjohann, K. L. Localized Corrosion of Low-Carbon Steel at the Nanoscale. *npj Mater. Degrad.* **2019**, *3*, 17.
(6) Dwivedi, D.; Lepková, K.; Becker, T. Carbon Steel Corrosion: A Review of Key Surface Properties and Characterization Methods. *RSC Adv.* **2017**, *7*, 4580−4610.
(7) Manuel, R. W. Effect of Carbide Structure on the Corrosion Resistance of Steel. *Corrosion* **1947**, *3*, 415−431.
(8) Sun, J. L.; Tang, H. J.; Wang, C. L.; Han, Z.; Li, S. S. Effects of Alloying Elements and Microstructure on Stainless Steel Corrosion: A Review. *Steel Res. Int.* **2022**, *93*, 2100450.
(9) Lyu, Z.; Yao, L. H.; Chen, W. X.; Kalutantirige, F. C.; Chen, Q. Electron Microscopy Studies of Soft Nanomaterials. *Chem. Rev.* **2023**, *123*, 4051−4145.
(10) Kosari, A.; Zandbergen, H.; Tichelaar, F.; Visser, P.; Taheri, P.; Terryn, H.; Mol, J. M. C. In-Situ Nanoscopic Observations of Dealloying-Driven Local Corrosion from Surface Initiation to In-Depth Propagation. *Corros. Sci.* **2020**, *177*, 108912.
(11) Yang, Y.; Shao, Y. T.; Lu, X.; Yang, Y.; Ko, H. Y.; DiStasio, R. A., Jr.; DiSalvo, F. J.; Muller, D. A.; Abruna, H. D. Elucidating Cathodic Corrosion Mechanisms with Operando Electrochemical Transmission Electron Microscopy. *J. Am. Chem. Soc.* **2022**, *144*, 15698−15708.
(12) Choi, B. K.; Kim, J.; Luo, Z.; Kim, J.; Kim, J. H.; Hyeon, T.; Mehraeen, S.; Park, S.; Park, J. Shape Transformation Mechanism of Gold Nanoplates. *ACS Nano* **2023**, *17*, 2007−2018.
(13) Liu, L. L.; Sassi, M.; Zhang, X.; Nakouzi, E.; Kovarik, L.; Xue, S. C.; Jin, B.; Rosso, K. M.; De Yoreo, J. J. Understanding the Mechanisms of Anisotropic Dissolution in Metal Oxides by Applying Radiolysis Simulations to Liquid-Phase TEM. *Proc. Natl. Acad. Sci. U.S.A.* **2023**, *120*, No. e2101243120.
(14) Wang, H.; Xu, Z.; Mao, S.; Granick, S. Experimental Guidelines to Image Transient Single-Molecule Events Using Graphene Liquid Cell Electron Microscopy. *ACS Nano* **2022**, *16*, 18526−18537.
(15) Hayden, S. C.; Chisholm, C.; Eichmann, S. L.; Grudt, R.; Frankel, G. S.; Hanna, B.; Headrick, T.; Jungjohann, K. L. Genesis of Nanogalvanic Corrosion Revealed in Pearlitic Steel. *Nano Lett.* **2022**, *22*, 7087−7093.
(16) Tian, M. K.; Choundraj, J. D.; Voisin, T.; Wang, Y. M.; Kacher, J. Discovering the Nanoscale Origins of Localized Corrosion in Additive Manufactured Stainless Steel 316L by Liquid Cell Transmission Electron Microscopy. *Corros. Sci.* **2022**, *208*, 110659.
(17) Kovalov, D.; Taylor, C. D.; Heinrich, H.; Kelly, R. G. *Operando* Electrochemical TEM, Ex-situ SEM and Atomistic Modeling Studies of MnS Dissolution and Its Role in Triggering Pitting Corrosion in 304L Stainless Steel. *Corros. Sci.* **2022**, *199*, 110184.
(18) Lestari, S.; Mäki-Arvela, P.; Beltramini, J.; Lu, G. Q. M.; Murzin, D. Y. Transforming Triglycerides and Fatty Acids into Biofuels. *ChemSusChem* **2009**, *2*, 1109−1119.
(19) Lange, J. P. Renewable Feedstocks: The Problem of Catalyst Deactivation and its Mitigation. *Angew. Chem., Int. Ed.* **2015**, *54*, 13186−13197.
(20) Krifa, M. Electrically Conductive Textile Materials-Application in Flexible Sensors and Antennas. *Textiles* **2021**, *1*, 239−257.
(21) Hack, H. P. Galvanic Corrosion. In *Shreir's Corrosion*; Elsevier: Oxford, 2010.
(22) Brewer, L. N.; Field, D. P.; Merriman, C. C. Mapping and Assessing Plastic Deformation Using EBSD. In *Electron Backscatter Diffraction in Materials Science*; Schwartz, A., Kumar, M., Adams, B., Field, D., Eds.; Springer: Boston, 2009; pp 251−262.
(23) Palisaitis, J.; Hsiao, C. L.; Junaid, M.; Birch, J.; Hultman, L.; Persson, P. O. Å. Effect of Strain on Low-Loss Electron Energy Loss Spectra of Group-III Nitrides. *Phys. Rev. B* **2011**, *84*, 245301.
(24) Shi, F. L.; Gao, W. P.; Shan, H.; Li, F.; Xiong, Y. L.; Peng, J. H.; Xiang, Q.; Chen, W. L.; Tao, P.; Song, C. Y.; Shang, W.; Deng, T.; Zhu, H.; Zhang, H.; Yang, D. R.; Pan, X. Q.; Wu, J. B. Strain-Induced Corrosion Kinetics at Nanoscale Are Revealed in Liquid: Enabling Control of Corrosion Dynamics of Electrocatalysis. *Chem* **2020**, *6*, 2257−2271.

(25) Wang, C. Y.; Du, K.; Song, K. P.; Ye, X. L.; Qi, L.; He, S. Y.; Tang, D. M.; Lu, N.; Jin, H. J.; Li, F.; Ye, H. Q. Size-Dependent Grain-Boundary Structure with Improved Conductive and Mechanical Stabilities in Sub-10-nm Gold Crystals. *Phys. Rev. Lett.* **2018**, *120*, 186102.
(26) Nnoka, M.; Jack, T. A.; Szpunar, J. Effects of Different Microstructural Parameters on the Corrosion and Cracking Resistance of Pipeline Steels: A Review. *Eng. Failure Anal.* **2024**, *159*, 108065.
(27) Sarochawikasit, R.; Wang, C.; Kumam, P.; Beladi, H.; Okita, T.; Rohrer, G. S.; Ratanaphan, S. Grain Boundary Energy Function for α Iron. *Materialia* **2021**, *19*, 101186.
(28) Cihal, V.; Kasova, I. Relation Between Carbide Precipitation and Intercrystalline Corrosion of Stainless Steels. *Corros. Sci.* **1970**, *10*, 875−881.
(29) Shimada, M.; Kokawa, H.; Wang, Z. J.; Sato, Y. S.; Karibe, I. Optimization of Grain Boundary Character Distribution for Intergranular Corrosion Resistant 304 Stainless Steel by Twin-Induced Grain Boundary Engineering. *Acta Mater.* **2002**, *50*, 2331−2341.
(30) Yao, L. H.; An, H.; Zhou, S.; Kim, A.; Luijten, E.; Chen, Q. Seeking Regularity from Irregularity: Unveiling the Synthesis-Nanomorphology Relationships of Heterogeneous Nanomaterials Using Unsupervised Machine Learning. *Nanoscale* **2022**, *14*, 16479−16489.
(31) Yoo, S. H.; Lee, J. H.; Jung, Y. K.; Soon, A. Exploring Stereographic Surface Energy Maps of Cubic Metals via an Effective Pair-Potential Approach. *Phys. Rev. B* **2016**, *93*, 035434.
(32) Jin, H. M.; Blackwood, D. J.; Wang, Y.; Ng, M. F.; Tan, T. L. First-Principles Study of Surface Orientation Dependent Corrosion of BCC Iron. *Corros. Sci.* **2022**, *196*, 110029.
(33) Yule, L. C.; Shkirskiy, V.; Aarons, J.; West, G.; Bentley, C. L.; Shollock, B. A.; Unwin, P. R. Nanoscale Active Sites for the Hydrogen Evolution Reaction on Low Carbon Steel. *J. Phys. Chem. C* **2019**, *123*, 24146−24155.
(34) Scribner, L. A. Corrosion by Organic Acids. In *CORROSION Houston*: Texas, 2001, pp 1−20..
(35) Saito, Y.; Utsunomiya, H.; Tsuji, N.; Sakai, T. Novel Ultra-High Straining Process for Bulk Materials-Development of the Accumulative Roll-Bonding (ARB) Process. *Acta Mater.* **1999**, *47*, 579−583.
(36) Mohtadi-Bonab, M. A. Effects of Different Parameters on Initiation and Propagation of Stress Corrosion Cracks in Pipeline Steels: A Review. *Metals* **2019**, *9*, 590.
(37) Gurrentz, J. M.; Jarvis, K. A.; Gearba-Dolocan, I. R.; Rose, M. J. Atomic Layer Deposited Al_2O_3 as a Protective Overlayer for Focused Ion Beam Preparation of Plan-View STEM Samples. *Ultramicroscopy* **2022**, *239*, 113562.
(38) Kosari, A.; Zandbergen, H.; Tichelaar, F.; Visser, P.; Terryn, H.; Mol, A. Application of In Situ Liquid Cell Transmission Electron Microscopy in Corrosion Studies: A Critical Review of Challenges and Achievements. *Corrosion* **2020**, *76*, 4−17.
(39) Yépez, O. On the Chemical Reaction Between Carboxylic Acids and Iron, Including the Special Case of Naphthenic Acid. *Fuel* **2007**, *86*, 1162−1168.
(40) Seo, S. H.; Park, J. H.; Kim, K.; Kim, T. H.; Kim, H. W.; Son, Y. S. Decomposition of Volatile Fatty Acids Using Electron Beam Irradiation. *Chem. Eng. J.* **2019**, *360*, 494−500.
(41) Neta, P.; Simic, M.; Hayon, E. Pulse Radiolysis of Aliphatic Acids in Aqueous Solutions. I. Simple Monocarboxylic Acids. *J. Phys. Chem.* **1969**, *73*, 4207−4213.
(42) Park, K. T.; Kim, Y. S.; Lee, J. G.; Shin, D. H. Thermal Stability and Mechanical Properties of Ultrafine Grained Low Carbon Steel. *Mater. Sci. Eng., A* **2000**, *293*, 165−172.
(43) Maleki, E.; Bagherifard, S.; Unal, O.; Bandini, M.; Farrahi, G. H.; Guagliano, M. Introducing Gradient Severe Shot Peening as A Novel Mechanical Surface Treatment. *Sci. Rep.* **2021**, *11*, 22035.
(44) Dumitrescu, L.; Maury, F. Al_2O_3 Coatings on Stainless Steel from Al Metal-Organic Chemical Vapor Deposition and Thermal Treatments. *Surf. Coat. Technol.* **2000**, *125*, 419−423.
(45) Vignesh, R. V.; Sathiya, P. Sacrificial Anode Materials to Protect Marine Grade Steel Structures: A Review. *Corros. Rev.* **2024**, *42*, 303−330.
(46) Jack, T. A.; Szpunar, J. Effect of Nb-Induced Microstructure on Pipeline Steel Corrosion and Stress Corrosion Cracking Performance in Acidic Environment. *Corros. Sci.* **2023**, *218*, 111196.
(47) Ralston, K. D.; Birbilis, N. Effect of Grain Size on Corrosion: A Review. *Corrosion* **2010**, *66*, 075005-1−075005-13.
(48) Pratt, V. Direct Least-Squares Fitting of Algebraic Surfaces. *ACM SIGGRAPH Comput. Graph.* **1987**, *21*, 145−152.

https://doi.org/10.1021/acsnano.5c06142
ACS Nano XXXX, XXX, XXX−XXX